American Mineralogist, Volume 59, pages 1–21, 1974

High Resolution Electron Microscopy of Silicates

PETER R. BUSECK, AND SUMIO IIJIMA[1]

Departments of Geology and Chemistry, and Department of Physics, Arizona State University, Tempe, Arizona 85281

Abstract

Imaging of crystal structures of minerals clearly shows details within ideally periodic regions, even at the unit cell scale. A variety of crystal imperfections can be observed at point-to-point resolutions down to 3Å—intermediate between bond lengths and unit cell dimensions. Fluctuations in both structure and composition can be observed in volumes up to 14 orders of magnitude smaller than is possible by standard single crystal X-ray techniques.

We have obtained crystal structure images of the following silicate structure types: "ring" structures (beryl and cordierite), isolated and paired tetrahedra (idocrase), single and double chains (orthoenstatite and hornblende), framework (scapolite), and sheet (muscovite). Regular and perturbed regions containing defects are clearly differentiable. Antiphase domains (hornblende) and stacking faults (enstatite) as well as the effects of radiation damage produce recognizable structural effects, only some of which are reflected in the electron diffraction patterns. An example of the usefulness of the technique is the resolution of small regions (several unit cells wide parallel to [100]) of clinoenstatite intergrown within orthoenstatite.

The technique of high resolution electron microscopy has great potential for mineralogy and geology. Solid solution series may well be resolvable into stoichiometric phases differing only slightly in both composition and/or structure. Homologous phases, potentially resolvable by electron microscopy, have the possibility of providing far more sensitive mineralogical indicators to past history and environments than currently exist.

Introduction

Fine details of mineral structures have long been successfully obtained by X-ray diffraction techniques. In spite of the unquestioned power of X-ray methods, there is no way that direct visual images of mineral structures can be obtained. Recent developments in high resolution electron microscopy (Allpress and Sanders, 1973) now permit the imaging of sets of unit cells[2] as well as some of the details within individual unit cells.

One-dimensional images of crystal structures have been obtained for some time, but these have primarily been used to demonstrate the stability of electron microscopes. Such studies produce images derived from two or three diffracted electron beams. These images are restricted to showing major periodicities of the crystals and, in general, the observed image contrast does not show a one-to-one correspondence with structure. Partly for this reason structure imaging methods have not been applied satisfactorily to mineralogical studies. Nonetheless, some structural information on minerals, for instance on asbestos (Yada, 1971) and montmorillonite (Yoshida and Suito, 1972), has been successfully obtained.

The use of electron microscopy for obtaining direct structural data from crystals was initiated by Allpress, Sanders, and Wadsley (1969) on the studies of some ternary Nb oxides. They observed abnormal lattice spacings when they imaged crystals by using a row of seven of the diffracted electron beams, rather than the two or three that previous investigators had used. Afterwards, this technique was extended to two-dimensional crystal structure images by Allpress (1970), Iijima (1971), and Iijima, Cowley, and Donnay (1973) who found that the images could be directly correlated with structural details. Iijima (1971) also shows metal atom positions within individual unit cells. The first direct

[1] On leave from the Research Institute for Scientific Measurements, Tohoku University.

[2] Such images have been called *lattice images* by electron microscopists. Properly speaking, they are the projected images of crystal structures and shall be called *structure images* in this paper.

structure determination from electron microscope images was performed by Iijima and Allpress (1973).

Using this technique it is possible to obtain point to point resolutions of 3Å and consequently to observe deviations from ideal structures. For example, information can be obtained on one or two dimensional defects and, in certain cases, on point defects (Iijima, Kimura and Goto, 1973). Depending on the material, it is also possible to observe short and long-range ordering, defect formation and propagation, twinning, and other phenomena occurring on the unit cell level.

Although we have investigated several minerals by this technique, we limit this paper to relatively well-known silicates that represent the major structure types. "Normal" rather than severely perturbed portions of crystals are generally illustrated. The images obtained with the electron microscope are related to structures determined from X-ray studies.

Electron Microscopy Versus X-Ray Diffraction

Electron beams are diffracted by electrostatic potential arising from both the nucleus and orbital electrons, while X-rays are diffracted only by the orbital electrons. Because an electron beam consists of charged particles it can be focussed to a small spot by electromagnetic lenses, whereas X-rays cannot be readily focussed. Consequently, by using electron beams we can concentrate high beam intensities onto very small areas.

The wavelength, λ, of electrons is determined by the non-relativistic relation $\lambda = 12.3 \times V^{-1/2}$Å, where V is the accelerating potential (in volts) for the electrons. For a 100 kV potential, typically used for transmission electron microscopy, $\lambda = 0.037$Å. In contrast, Cu$K\alpha$ X-rays have $\lambda = 1.54$Å, almost two orders of magnitude greater. As a consequence the Bragg angle, θ, is much smaller for electron than for X-ray diffraction. This results in an increase in the number of planes that simultaneously fulfill the Bragg condition. In other words, the radius $(1/\lambda)$ for the Ewald sphere is so much larger for electron diffraction that its surface more closely approaches a plane and thus can more nearly coincide with a plane of the reciprocal lattice. By contrast, for X-rays one must go to complicated precession motions to obtain similar planar sections in reciprocal space. By using electron microscopes having higher accelerating potentials, the radius of the Ewald sphere is even larger and more reflections can be recorded.

Interaction of the electrons with atoms is much stronger than for X-rays. Consequently, double or multiple diffraction of the electrons commonly produces some "forbidden" reflections. This becomes a particularly serious problem for thick specimens. Another problem is the effect of absorption produced by inelastic scattering. The combined effect of these factors makes the interpretation of electron diffraction patterns difficult. Thus, a dynamical treatment for diffraction is required (*e.g.,* Cowley and Moodie, 1957) rather than the kinematical treatment that is used for X-rays.

Although the physics of electron diffraction is more complicated than for X-rays, there are several advantages to using electrons. The electron diffraction patterns are immediately visible on a fluorescent screen, rather than requiring extended photographic exposures. Also, electron diffraction patterns are easily obtainable from very small specimens ($\sim$1 μm diameter). A great additional advantage of electron microscopy is that electron images can be obtained from the diffracted beams.

A desirable feature of electron microscopy is that the data are not averaged over nearly as many unit cells as for X-rays. For example, X-ray information is generally obtained from crystals at least 0.1 mm on a side, *i.e.,* crystals having a volume $>10^{18}$ Å^3. By contrast, the type of electron microscopy that is described in this paper can provide data from areas smaller than 10Å on a side and $\sim$150 Å thick, *i.e.,* a volume of $<10^4$ Å^3. In other words there is a difference of at least 14 orders of magnitude in the volumes studied! This means that fine structure that is averaged out by X-rays can be resolved and observed with electrons. The great advantage of X-rays is this ability to average structure over relatively large volumes. The most important single advantage of electrons is the ability to observe localized fine detail.

The small crystal volumes observed by electron imaging can also lead to problems as they need not be representative of the crystal as a whole. Care must be exercised to ensure that images are obtained in a sufficiently large number of places in the crystals to determine which images are representative.

The images observed by electron microscopy are to a first approximation related to the corresponding electron diffraction patterns through their Fourier transforms. This process can be understood in terms of Figure 1. The expression for the beam transmitted through the specimen is given as a transmission

function $f(x, y)$, where x and y are the Cartesian coordinates for all points on the crystal, relative to a set of arbitrary axes. If we have a very thin crystal the specimen can be regarded as a phase object, *i.e.,* there is negligible absorption and so the wave amplitude does not change during electron transmission, only its phase does. In this case

$$f(x, y) = e^{-i\sigma\phi(x,y)} \tag{1}$$

where σ is the interaction constant (dependent on the accelerating voltage of the microscope: $\sigma = \pi/V\cdot\lambda$), and $\phi(x, y)$ is the electrostatic potential distribution within the crystal, projected along the direction of the electron beams; the value of $f(x, y)$ can be calculated from this relationship.

The diffraction pattern can be described as the Fourier transform $F(u, v)$ of the transmission function, analogous to the X-ray diffraction pattern being the Fourier transform of the electron density. Electron microscopy differs, of course, in that an electron image can also be formed. Under ideal conditions the image seen in the Gaussian image plane of the objective lens (assuming no spherical aberration, observationally the plane where the Fresnel fringe, similar to the Becke line of optics, is absent) is the Fourier inverse transform of the diffraction pattern. Since the transform of the transform is the original function (neglecting inversion and magnification), the image would correspond to the original transmission function

$$\psi(x, y) = \mathfrak{F}\{F(u, v)\} = f(x, y) \tag{2}$$

where $\psi(x, y)$ is the wave function (amplitude), positioned in the image plane. Under actual operating conditions, however, the image cannot be considered as a simple Fourier transform because of several instrumentally introduced effects. Thus, the diffraction function, $F(u, v)$, is modified by a phase term, $e^{i\chi}$, and an objective aperture function, $A(u, v)$, so that the resulting relationship takes the form

$$\psi(x, y) = \mathfrak{F}[F(u, v)\cdot e^{i\chi}\cdot A(u, v)] \tag{3}$$

The phase term, $e^{i\chi}$, is introduced by spherical aberration of the objective lens, and optical defocussing. The spherical aberration causes phase delay between the direct and diffracted beams. A phase delay also results from small changes in the focal length of the objective lens that are produced during the defocussing required for proper image formation. For a given set of operating conditions χ is constant and can be evaluated.

The objective aperture function, $A(u, v)$, is the result of the insertion of a screen with a hole centered around the direct electron beam. This is required to stop the higher order diffracted beams, as they suffer increased phase change which increases the background noise. The aperture limits the number of diffracted beams which contribute to the image and therefore the information. The value of $A(u, v)$ is 1 for each beam that is allowed to pass through the aperture and 0 for those beams that are blocked.

The expression for the image at optimum defocus can now be determined by taking the Fourier transform of the corrected diffraction function. An approximation of the resulting expression for the intensity, $I(x, y)$, in the image plane is

$$I(x, y) = \psi\psi^* = 1 + 2\sigma\phi(x, y), \tag{4}$$

where $\phi(x, y)$ is the expression for the electrostatic potential distribution in the crystal, and ψ^* is the complex conjugate of ψ. This relationship roughly approximates the image contrast in the electron micrographs of the crystal structures shown in the following pages (Cowley and Iijima, 1972; Allpress

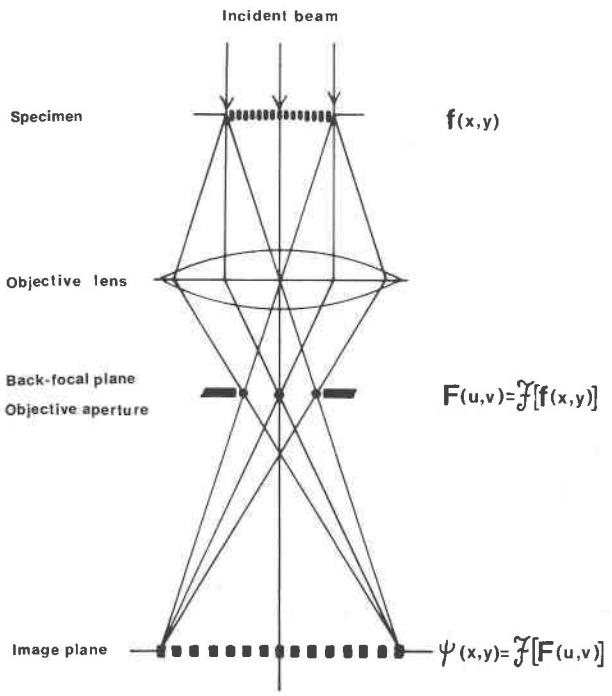

FIG. 1. Schematic diagram of image formation by the objective lens of the transmission electron microscope. The mathematical functions appropriate to the various positions are indicated; see text for details.

and Sanders, 1973). In other words, using electron microscopy we can see the projected structure directly.

The contrast observed in the electron image derives from electrostatic potential differences in the crystal. If heavy atoms are present then they make a major contribution to the image contrast. Thus, on the (photographic) projections shown in this paper dense rows or columns of heavy atoms or other regions of high electrostatic potential appear dark, and low atomic number atoms or regions appear light. If the projected distances between the heavy atom positions are sufficiently large compared with the resolution of the microscope (~3 Å in our instrument), they are imaged as separated dots. Otherwise they are smeared into large blobs. In the case of a mineral such as beryl, which contains only light elements, the contrast in the electron image is developed between the empty channels and the surrounding atoms.

Experimental

Specimens are crushed to a fine powder (a few microns in diameter), dispersed in an ultrasonic bath, and suspended in acetone. They are then deposited on copper grids which have been pre-coated with a "holey supporting film." This is prepared by dissolving Formvar in ethylene dichloride, coating a glass slide with the solution, placing it over steam to produce the small holes, and then finally transferring the film from the glass slide to the grids.

A JEM-100B electron microscope (operated at 100 kV) with a high resolution goniometer stage is used. By combining a rotation and tilting operation, this stage permits tilting up to 30° from horizontal in any direction. Such goniometry is of critical importance for obtaining the proper orientations of the crystal.

The microscope has been modified in several ways: an extra anticontamination device has been added to the specimen chamber, a pointed filament is used to obtain added resolution and brightness, and the specimen position on the tilting stage has been lowered in order to increase magnification and resolution.

In order to obtain good structural information from the electron image, the specimen thickness should not exceed ~150 Å. Before tilting, the orientation of the specimen should lie within 25-30° of the desired position relative to the electron beam. Considerable time is generally spent in locating a crystal that is suitable in orientation and thickness for studying the particular features of interest.

A thin portion of the crystal should project over one of the holes in the supporting film. This minimizes electron beam interaction with extraneous material. Once located, the crystal must be tilted and rotated so that the appropriate zone axis is less than 0.5° from coincidence with the electron beam, *i.e.*, the reciprocal lattice section is perpendicular to the beam. In the case of zone [*uvw*], reflections *hkl* that fulfill the criterion $hu + kv + lw = 0$ will appear. For example, for [100] coincident with the electron beam, the set of reflections 0*kl* will be in a proper Bragg diffraction position.

Proper orientation is obtained by viewing the diffraction pattern during tilting. If the intermediate lens is defocussed slightly the crystal of interest can be viewed within the diffraction spots and its position adjusted so it does not move out of the field during tilting. After critical beam alignment, insertion of the objective aperture and stigmating of lenses, structure images can be viewed at 4.2×10^6 times magnification on the fluorescent screen of the microscope. To produce maximum information as many diffracted beams as possible should be included in the aperture. However, diffracted beams far from the optical axis suffer much phase delay because of spherical aberration of the objective lens and therefore should be excluded. From our experience an aperture of 50 μm diameter (corresponding to a radius of ~2.6 $Å^{-1}$ in the electron diffraction pattern) gives the best results.

Optimum images for structural detail are obtainable at a critical value of underfocussing of approximately 900 Å relative to the Gaussian image plane. To insure that we viewed the optimum image, through-focus images were recorded at various focusing conditions for all specimens. The orienting and matching of the lattice images with structures determined with X-rays can then be done. Measured spacings and symmetry of the image are compared to the corresponding reflections on the electron diffraction patterns and the correspondence determined.

In high resolution microscopy, it is common that the specimens suffer radiation damage or heating effects from the extremely intense electron beam irradiation. Therefore there is always concern as to whether the images represent original, unperturbed structures even if recorded as rapidly as possible with beams having minimal intensities. We generally did not recognize appreciable changes in the image

contrast during observation and thus believe that most of the presently described specimens did not suffer significant radiation damage. Some minerals that we wished to study, however, were unsuitable because of their rapid decomposition under the beam. In order to be usable for study, the mineral in question must be stable in a vacuum and should neither melt nor degrade in the electron beam.

Results

A few minerals belonging to the major silicate groups were selected to explore this technique of structural imaging. Beryl and cordierite were chosen because they contain six-membered rings of tetrahedra. Recent investigators (Zoltai, 1960; Gibbs, 1966; Gibbs *et al,* 1968) point out that these minerals are actually framework structures because the six-membered rings are strongly cross-linked by tetrahedrally coordinated cations. The present technique nicely illustrates these six-membered rings. Also examined were idocrase, which contains isolated and double tetrahedral groups; hornblende and orthoenstatite, which respectively contain double and single chains; scapolite, which has a framework structure; and muscovite, a sheet silicate.

Beryl

Beryl ($Al_2Be_3Si_6O_{18}$) is a commonly used example of an important mineral containing rings of SiO_4 tetrahedra. The structure was originally described by Bragg and West (1926); it has a close to and c equal to 9.2 Å and belongs to space group $P6/mcc$. It consists of 6-membered rings connected by Be in 4-fold coordination and Al in 6-fold coordination (Fig. 2). The Be is located between each set of two adjacent rings and the Al between each set of three adjacent rings. Large open channels are centered about the 6-fold axes. No atomic center is nearer than 2.55 Å to the centers of these channels.

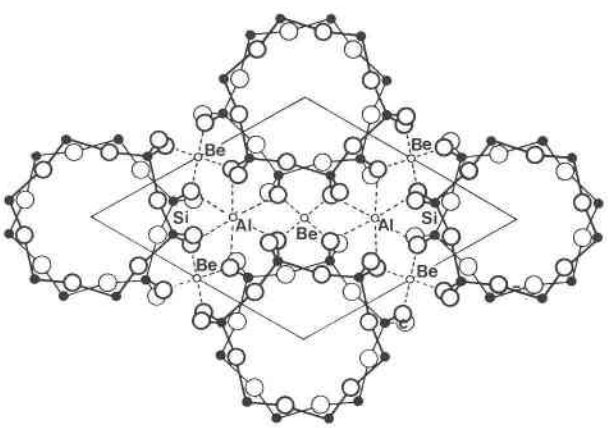

FIG. 2. The structure of beryl, projected on (001). The unit cell is outlined by the parallelogram (after Bragg and West, 1926).

Zoltai (1960) and Gibbs, Breck, and Meagher (1968) have pointed out that beryl should be considered a framework structure because of the tetrahedrally coordinated Be linking the rings. Such a structural reclassification of the silicates does not affect the present discussion.

Figure 3a, at a magnification of 2.7×10^7X, shows a structure image of a portion of a baby blue colored crystal from a Hermosillo, Mexico, pegmatite. It is oriented with its c axis coincident with the electron beam. A unit cell, having a 9.2 Å edge, is outlined. The prominent white areas represent the large open channels. The surrounding areas, containing a higher concentration of electrostatic potential, are dark. The inset, at the same scale as the electron image, shows the X-ray structure of several unit cells. Note that many of the channels appear to be irregularly shaped and even triangular, rather than having the round outlines shown in the X-ray structure. Much of this deviation from roundness is probably the result of statistical fluctuations or noise; some of the distortion is below our limit of resolution. Nonetheless, it is probable that a portion of the deviation of channel shape results from a non-circular distribution of the electrostatic potential.

Figure 4 shows an image of the crystal oriented at right angles to the view shown in Figure 3a. For this orientation the long channels can be seen running parallel to c. The inset on Figure 4 shows the corresponding electron diffraction pattern with the outline of the objective aperture indicated by a white circle. Only the beams within this circle were utilized for producing the image and therefore contributed information to it.

Cordierite

The structure of cordierite, first described by Gossner and Mussgnug (1928), is similar to that of beryl. However, the six-membered Si_6O_{18} ring in beryl becomes an $Al_2Si_4O_{18}$ ring in cordierite, the Al being ordered at opposite sides of the ring (Fig. 5). This reduces the symmetry from hexagonal to orthorhombic ($a = 17.1$; $b = 9.7$; $c = 9.3$Å; $Cccm$). The Si_6O_{18} rings in beryl are cross-linked by Al in octahedral sites and by Be in tetrahedral sites, whereas in

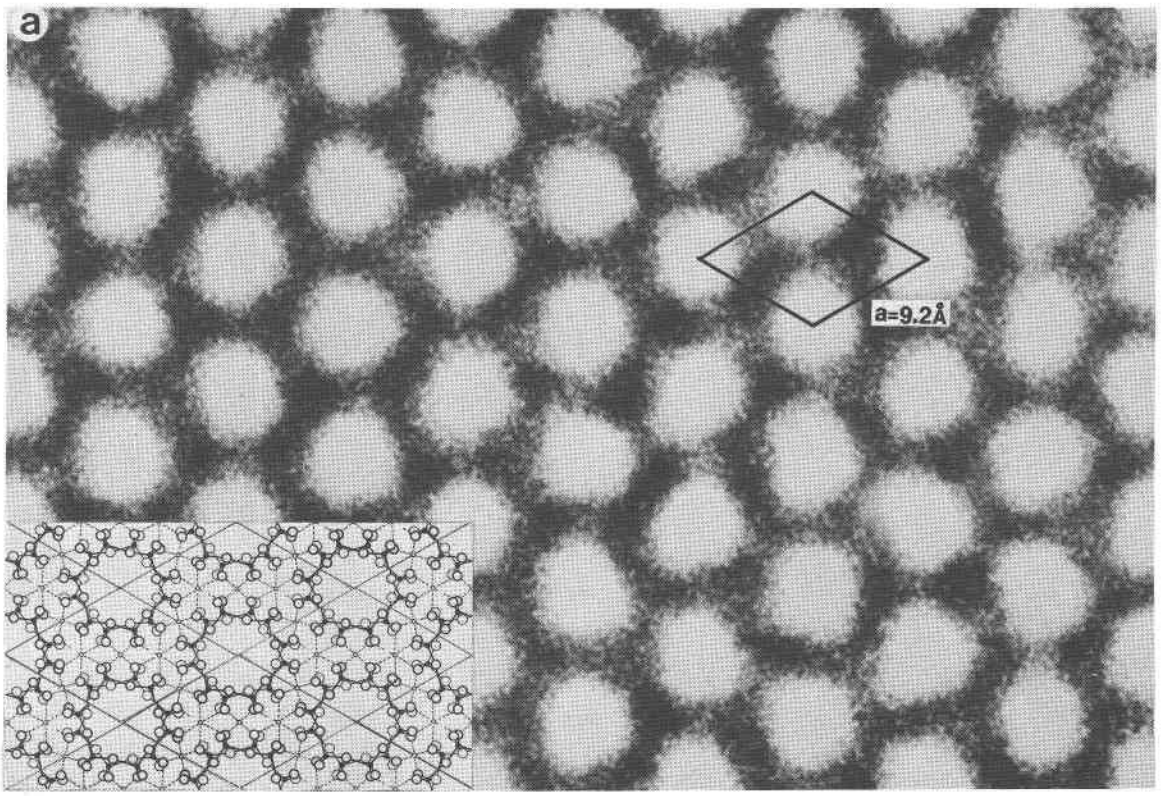
a
a=9.2Å

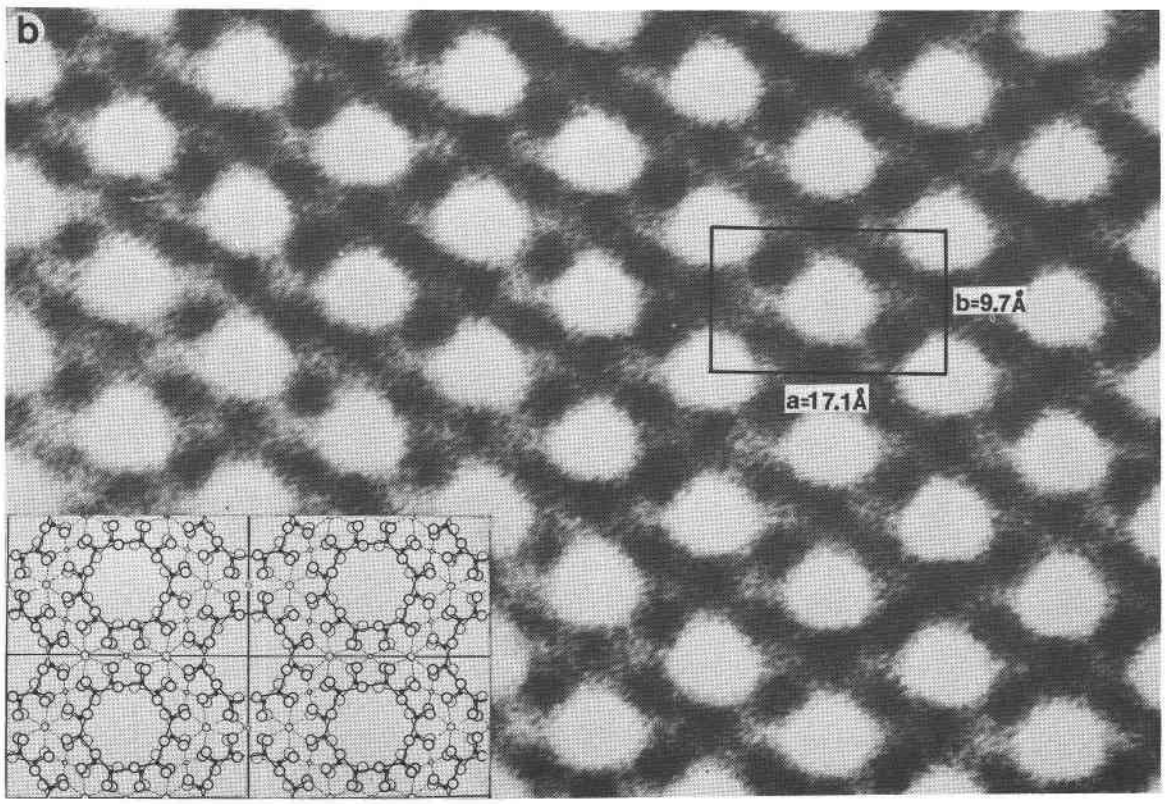
b
b=9.7Å
a=17.1Å

cordierite the cross-linking is by Mg in octahedral sites and by an ordered distribution of Al and Si in the tetrahedral sites. Because of the greater possibility of ionic substitution in cordierite than in beryl, problems of ordering are more complex.

Considerable attention has been given to the question of order-disorder, its relationship to polymorphic transitions, and the structural significance of the "distortion index" (Miyashiro, 1957; Gibbs, 1966; Meagher and Gibbs, 1965; Langer and Schreyer, 1969; Fontaine, 1969). In most cases cordierites that formed at lower temperatures are more ordered, and have a higher distortion index, than those that formed at higher temperatures. This is mainly due to Al/Si disorder, but possibly also depends on interchange between Al and the cations in the octahedral sites (Mg, Fe, Mn). Langer and Schreyer (1969) suggest that both long- and short-range order may account for the ambiguous interpretations of the distortion index. Hopefully, future high resolution electron microscopy will be able to help unravel some of the complications.

A sample of cordierite from Garleburg, Sweden, was studied. Its composition is indicated in Table 1. Its formula, $(Mg_{1.6}Fe_{0.3}Al_{0.1})Al_4Si_5O_{18}$, compares well with the theoretical or idealized formula $(Mg,Fe)_2Al_4Si_5O_{18}$. This analysis, as well as the others in this paper, was done on an electron microprobe using mineral or synthetic oxide standards. The operating potential was generally 15kV using a specimen current of 40 namp. Four elements were measured simultaneously for a given mineral. The normal computer corrections for absorption, fluorescence, atomic number, dead time, and drift were applied to the raw analytical data.

Figures 3a and 3b show the beryl and cordierite structure images at the same scale. Note the strong similarity in appearance. As in beryl, the most obvious features of the cordierite structure are the large open channels. Also prominent, however, are the black spots located between each set of two adjacent channels. These correspond to the positions

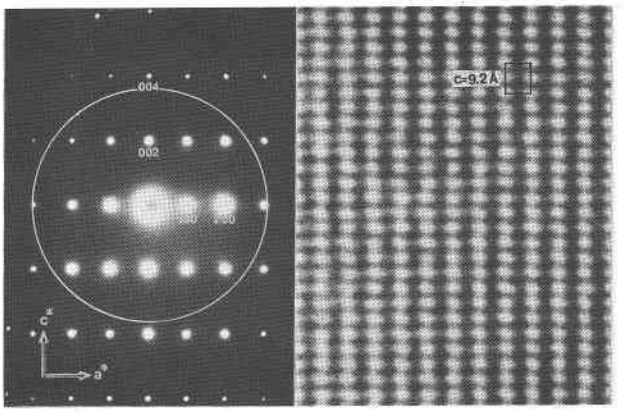

FIG. 4. Structure image of an *a-c* section of beryl. The electron diffraction pattern is shown on the left. The projected position of the objective aperture is outlined by a white circle.

of the tetrahedrally coordinated Al and Si atoms cross-linking the $Al_2Si_4O_{18}$ rings. Their greater abundance and slightly higher atomic number than Mg, combined with the relatively greater proximity of oxygen and Si atoms in the rings, explain the prominent contrast of the region of the tetrahedral, cross-linking sites relative to the adjacent, octahedrally coordinated Mg. Presumably the octahedral sites would be distinguishable in an Fe-rich cordierite.

To obtain a correct structural representation of a crystal, the correct orientation, focus, and crystal thickness are required. The effect of changing focus is illustrated in Figure 6a, which shows a through-focus series of images. The steps in focus are equal to ~450 Å. Note the profound changes in contrast that are produced by such small focal variations. The

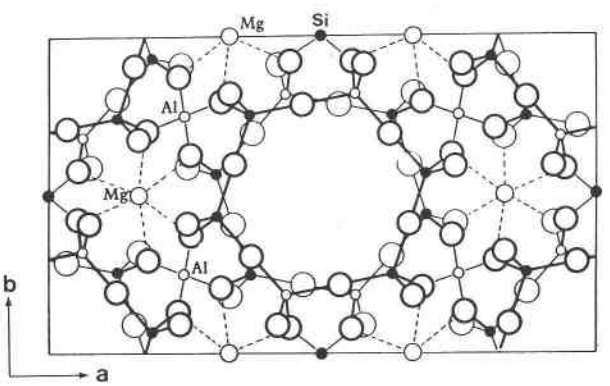

FIG. 5. The structure of cordierite, projected on (001). The unit cell is outlined; note the similarity to the beryl structure and the slight distortion that produces the orthorhombic unit cell (after Gibbs, 1966).

FIG. 3. a. High magnification structure image of beryl showing projection perpendicular to [001]. A unit cell is outlined; the insert shows the idealized beryl structure from Figure 2, at the same scale as the electron image.

b. High magnification structure image of an *a-b* section of cordierite. A unit cell is outlined; the insert shows the idealized cordierite structure from Figure 5, at the same scale as the electron image.

TABLE 1. Electron Microprobe Analyses

Oxide	Garleburg CORDIERITE Wt. %	CP**	Thetford IDOCRASE Wt. %	CP	CP-T†	Norton County ENSTATITE Wt. %@	CP	San Carlos HORNBLENDE Wt. %	CP	Otter Lake SCAPOLITE Wt. %	CP	CP Al+Si=12	CP-T†	Oxide
SiO_2	49.5	4.97	38.2	17.7	18	59.0	.98	40.6	5.96	50.5	7.37	7.70		SiO_2
TiO_2			.04	.01		.1	< .01	4.7	.52				12.0	12 TiO_2
Al_2O_3	34.3	4.06	19.6	10.7	8	.1	< .01	13.7	2.37	23.9	4.11	4.30		Al_2O_3
Fe_2O_3								4.1	.45					Fe_2O_3
FeO	4.1	.344	1.3	.5	5	.1	< .01	12.2	1.50	.14	.02	.02		FeO
MnO			.14	.05		.1	< .01	.3	.04					MnO
MgO	10.9	1.63	2.5	1.7		40.3	1.0	9.8	2.15					MgO
CaO			36.8	18.2	19	.3	.01	10.1	1.59	11.9	1.86	1.94	3.95	4 CaO
Na_2O			.03	.02				3.1	.89	5.94	1.68	1.76		Na_2O
K_2O			.004	.003				1.1	.21	1.20	.22	.23		K_2O
CO_3										2.6@	.38	.40		CO_3
SO_3										.79	.09	.09	.91	1 SO_3
Cl										1.62	.40	.42		Cl
O*		18		72	72		3		23		24			O*
Sum	98.8		98.6			99.6		99.7		98.7				Sum

*Number of oxygen atoms used for the calculation of the cationic proportions.
**CP = Cationic Proportion
†Based on the idealized composition.
† CP-T = Theoretical Cationic Proportion
@Reid and Cohen (1967)
©Carbon was not analyzed. From stoichiometry ($\frac{Ca+Fe}{4}$ - S for Al + Si = 12) there should be no more than .40 atomic proportions of C.

contrast is entirely reversed between −900 and +450 Å. Only at an underfocus of roughly 900 Å will the correct image result. At other focal values seriously misleading interpretations are possible.

Figure 6b was taken using a wedge-shaped crystal. The structure image of the crystal clearly shows the effect of thickness. Note that the quality of the image degrades with increasing thickness and, indeed, is distinctly deceptive for structural information. Only at the thin edge of the crystal (<150 Å thick) will a correct representation of the structure be obtained.

Idocrase

The structure of idocrase ($a = 15.5$, $c = 11.8$ Å, and probable space group $P4/nnc$) is considerably more complex than either of the previous examples. It is "one of a small number of rock-forming silicates whose formula and structure are not fully established" (Ito and Arem, 1970). A (001) projection (after Warren and Modell, 1931) is shown in Figure 7. There is some uncertainty regarding the detailed structure. According to Warren and Modell it consists of three types of channels running parallel to c. In the idealized structure each unit cell contains channels that we shall call "R" and contain 2 Ca + 2 Si atoms, channels of type "S" contain 2 Ca, and those of type "T" contain 2 Mg or Fe. These channels extend infinitely through the crystal. Coda *et al* (1970), however, report that the "S" channels contain only 1 Ca + 1 Mg or Fe. Arem and Burnham (1969) point out that there is additional ambiguity in that idocrase crystallizes with several space groups.

The channels are surrounded by roughly spirally-arranged SiO_4 tetrahedra, both in isolated SiO_4 groups and in double Si_2O_7 corner-sharing tetrahedra. In a (001) projection these tetrahedra are clustered in four-leafed clover patterns consisting of four groups of tetrahedra. Above or below (in the c direction) each of the silicons is a Ca atom. The net effect is that each "S" channel is surrounded by a clover of four Si–O–Ca clusters containing high atomic potential. The clovers are joined to one another by tetrahedrally coordinated Al. Rows containing the Al atoms and running through the "R" and "T" channels are parallel to ⟨110⟩, forming a square pattern.

The structure image of this rather complicated material is shown (Fig. 8) for a clear, light apple-green idocrase crystal from the Johns Manville mine, Thetford, Quebec. It is oriented with its c axis coincident with the electron beam. The insert in the lower corner of the figure shows four unit cells of idocrase on the same scale as the electron image. The shaded stripes that have been added to the inset parallel ⟨110⟩, along the Al sites where the Al connects the clovers surrounding the "S" channels. These stripes also clearly emphasize the positions of the "S" clovers. In the structure image the high atomic potential clovers are immediately apparent as the clustered dark areas around the white spots. The latter

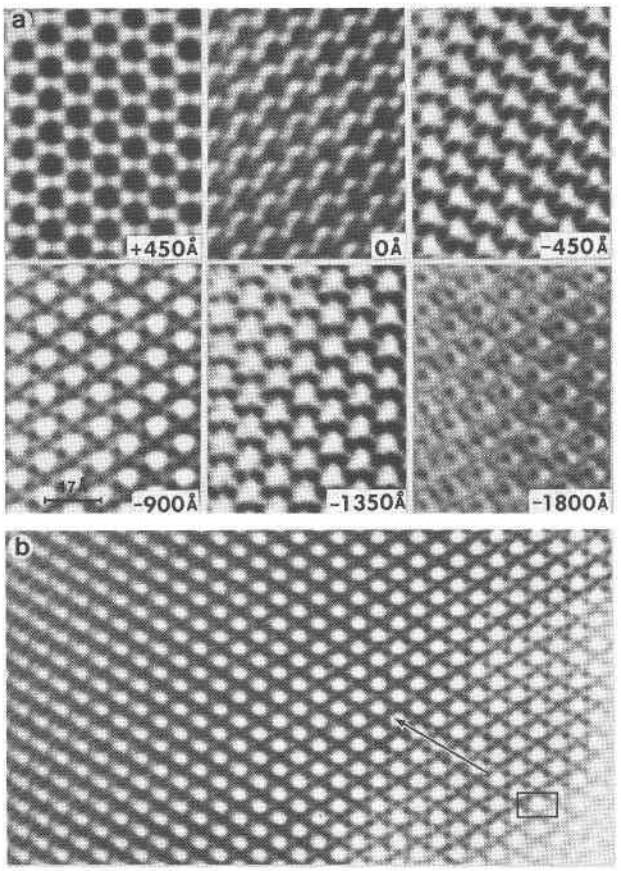

FIG. 6. a. Through-focus series of structure images of cordierite, showing the great sensitivity of the electron image to the position of focus. A good correspondence with structure is obtained at an underfocus of 900 Å (*cf* Fig. 3b). Note the reversal in contrast between +450 and −900 Å.

b. Structure image of a wedge-shaped crystal of cordierite showing the sensitivity of the image to changes in crystal thickness. The crystal is at least a few hundred Ångstroms thick at the thick side. The arrow points in the direction of increasing thickness. Note that structure is only correctly represented at the thin edge.

represent the "S" channels. The "R" channels are diagonally placed relative to "S". The light gray stripes parallel to ⟨110⟩ connect the "R" and "T" channels and include the intermediate, tetrahedrally coordinated Al atoms that connect the clovers to one another.

In parts of the crystal there is a contrast difference between the white spots representing the "S" channels and the grayer "R" channels. According to the idealized composition and structure of Warren and Modell (1931) there is only a difference of 2 Si in channel occupancy between "R" and "S". In the model of Coda *et al* (1970) a heavy Ca is replaced by an Mg (or Fe) atom in the "S" channels. The measured composition of the Thetford idocrase (Table 1) helps explain but does not uniquely resolve the apparent discrepancy in both composition and contrast.

Several idealized compositions have been proposed for idocrase, but none is totally consistent with any other. Of the two most recently proposed formulae (Coda *et al,* 1970, and Ito and Arem, 1970), our specimen corresponds more closely to that of Coda *et al.* Their idealized composition, corrected for OH, for a half unit cell is Ca_{19} (Mg, Fe, Al)$_5$ $Al_8Si_{18}O_{72}$, whereas we obtain $Ca_{18.2}$ $(Mg_{1.7}Fe_{0.5}Al_{2.4})Al_8(Si_{17.7}Al_{0.3})O_{72}$ (Table 2). Relative to the idealized composition, our specimen shows a deficiency of 0.8 Ca and 0.4 (Mg + Fe + Al) per half unit cell. If these vacancies were selectively ordered into the "S" channels, then a decrease in electrostatic potential and an increase in image contrast would be predicted. Theoretical calculations are required to determine whether the magnitude of the predicted image contrast corresponds to that in Figure 8.

Figure 9a is at lower magnification than Figure 8; it shows the regularity and freedom from major de-

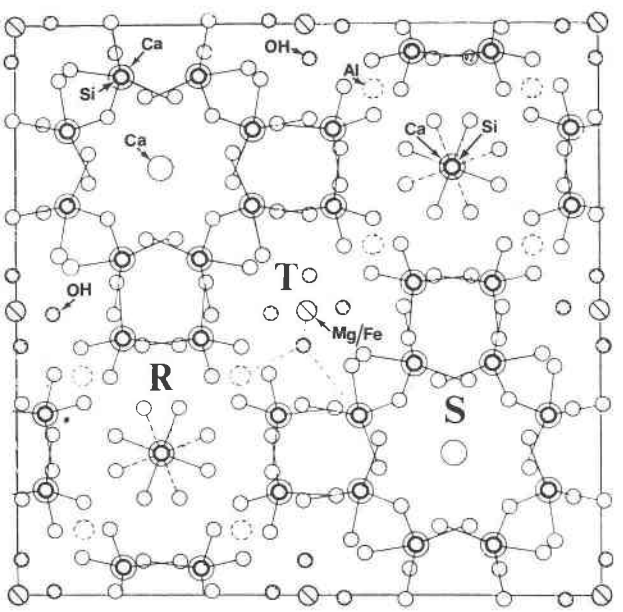

FIG. 7. The structure of a unit cell of idocrase, projected on (001) (after Warren and Modell, 1931). The nature of the channels at "R", "S", and "T" are explained in the text. The small open circles represent oxygens, the large open circles Ca, the small heavy circles Si.

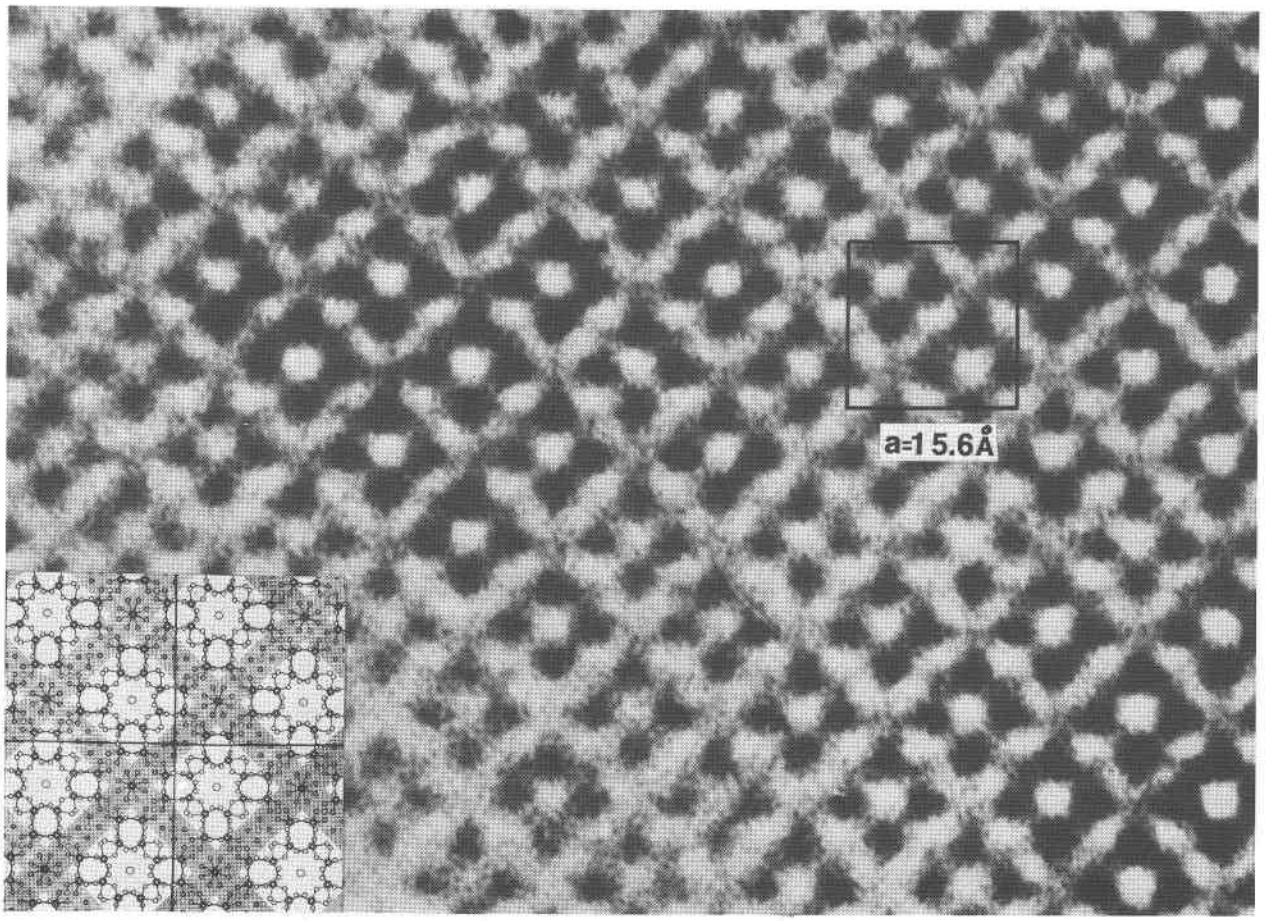

FIG. 8. High magnification structure image of idocrase showing a section perpendicular to *c*. A unit cell is outlined ,and the insert shows several cells from Figure 7 at the same scale as the structure image. The projected zones containing Al sites and the "R" and "T" sites have been shaded slightly.

fects of an appreciable portion of the crystal. Note, however, the change in image contrast toward the thicker portions of this wedge-shaped crystal. Although symmetry is maintained throughout, the correct structure appears only along the thin (~150 Å) edge of the crystal (on the right). A similar effect occurs for other crystals as well (*cf* Fig. 6b).

An electron diffraction pattern of idocrase is shown in the upper left corner of Figure 9a. Note that it contains weak "forbidden" reflections of the type 100. These presumably result from idocrase belonging to a space group other than the one indicated previously, perhaps because of the presence of antiphase domains.

Idocrase illustrates another feature that may be encountered in the electron microscopy of minerals—radiation damage. The high energies and heating produced by the electron beam destroy some crystals so rapidly that microscopy using present techniques is precluded. Other crystals decompose more slowly. Figure 9b shows the appearance of a crystal after roughly 20 minutes exposure to a 100 kV electron beam. Note the prominent control exerted along ⟨110⟩, reflecting the weaker bonding between the columns of "S" channels. This zone of failure contains the OH positions.

Orthoenstatite

Orthoenstatite is a chain silicate having $a = 18.22$, $b = 8.83$, and $c = 5.19$ Å, and belonging to space group *Pbca*. The long single chains of linked SiO_4 tetrahedra in orthoenstatite are joined by cations in two types of sites, M_1 and M_2 (Figure 10a). Enstatite from the Norton County achondritic meteorite was selected for this study. Its composition, indicated in Table 1, shows it to be En_{100}. A structure image taken with *c* oriented parallel to the electron beam (Fig. 11a) shows an orthogonal pattern of white

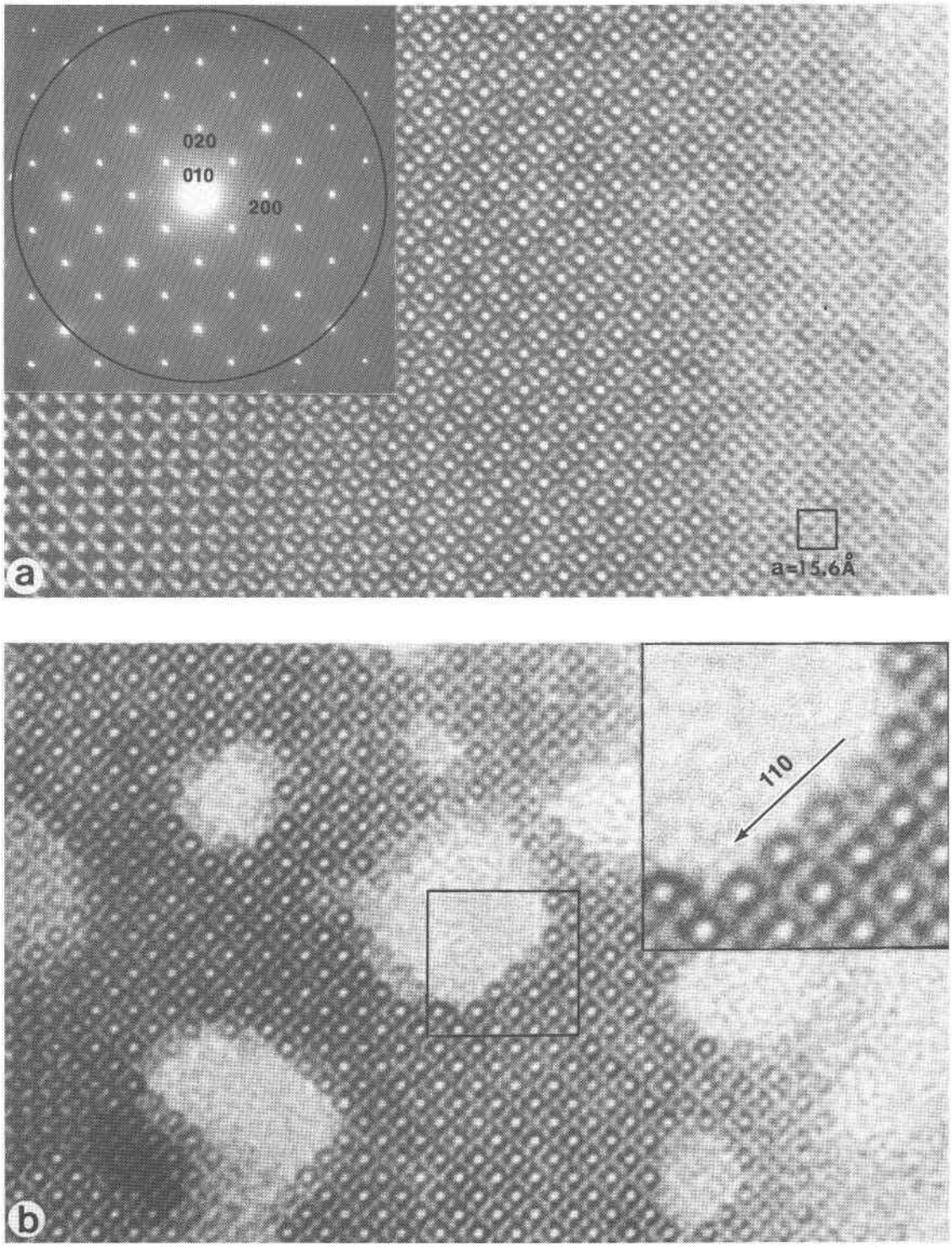

FIG. 9. a. Intermediate magnification structure image of a wedge-shaped crystal of idocrase. Note that the symmetry is maintained towards the thicker regions (to the left), but that the contrast changes appreciably so that structure is no longer directly interpretable. An electron diffraction pattern is shown on the left. Note the weak "forbidden" $h + k$ odd reflections.

b. Structure image of idocrase showing the effects of radiation damage. This occurs preferentially along [110], where the "S clovers" are joined by aluminums.

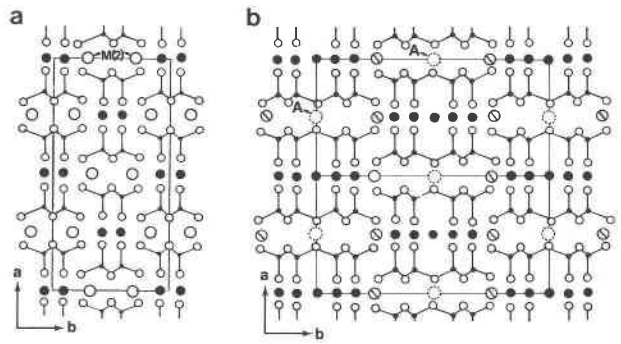

FIG. 10. Schematic structure of an *a-b* section of (a) orthoenstatite and (b) an amphibole, *e.g.,* hornblende. The large open circles represent oxygen atoms; the small black dots, Si; the large black dots, the M_1 sites in orthoenstatite and the M_1, M_2, and M_3 sites in amphibole. The orthoenstatite M_2 sites are shown as large open circles and the amphibole M_4 and "A" sites are represented as slashed circles and dotted circles, respectively.

spots. The characteristic rectangular cleavage of pyroxene is easily visualized from this pattern and the black line on the figure outlines such a possible cleavage surface (according to the model of Warren, 1929). The white spots in Figure 11a correspond to the areas where the chains are "back to back", indicating that, as expected, there is relatively lower electrostatic potential between the M_2 sites than elsewhere in the structure. The unit cell of orthoenstatite is marked on the figure. The *a* direction would be halved if this were either the clino- or protoenstatite polymorph.

Single crystal X-ray patterns have been reported as showing one or more of the following—diffuse spots, streaking, or extra spots—while powder patterns commonly show diffuse lines. There has been much discussion in the literature that these features result from stacking faults. Brown and Smith (1963) suggested that one possibility for the disorder is that stacking faults occur at the edges of blocks of orthoenstatite that formed from differing nuclei during the transition from a high temperature form.

An alternate explanation is that there are included areas of clinoenstatite. The literature discussing the $MgSiO_3$ polymorphs and their interrelationships has been reviewed by Smith (1969). Of the three geologically significant $MgSiO_3$ polymorphs, it appears that clinoenstatite is metastable at low temperatures, being transitional between protoenstatite, stable at high temperatures, and orthoenstatite, the stable low temperature form. Clinoenstatite can be formed by rapid cooling of protoenstatite (Brown, Morimoto, and Smith, 1961). An alternate mechanism for its formation was suggested by Turner, Heard, and Griggs, (1960), who reported that there is a stress-induced transition of orthoenstatite to clinoenstatite, with translation on (100) parallel to [010]. Had the Norton County enstatite been shocked, such clinoenstatite would be expected.

The Norton County meteorite is brecciated and contains evidence of shock. Reid and Cohen (1967) speculate that this caused probable intergrowths of orthoenstatite and clinoenstatite. Earlier, Brown and Smith (1963) and Pollack and Ruble (1964) pointed out that the Norton County enstatite is disordered, and Pollack (1966) in fact noted disorder in a relatively large number of other meteorites.

Figure 12a shows a section of enstatite that is orthogonal to the one illustrated in Figure 11a, *i.e., c* lies within the plane of the figure. The long subparallel fringes show the relative positions of the silicate chains. Note the discontinuities between the chains and the resulting irregular sequence of stacking faults with their planes parallel to *c*.

Figures 13a and 13b show electron diffraction patterns corresponding to a [001] projection (Fig. 11a) and a [010] projection (Fig. 12a). Note the streaking in Figure 13b; we believe that this is the result of the stacking disorder produced by the coherent interleaving of blocks of ortho- and clinoenstatite. Figure 13b shows "forbidden" spots of the type $h00$ where h is odd. This is the result of multiple diffraction, as well as containing a possible contribution from the presence of antiphase domains.

Measurement of the fringes lying parallel to the $a - b$ plane shows consistent spacings of ~18 Å except where irregularities occur. There the spacings are in 9 Å multiples, indicated by arrows in Figure 12a. The 18 Å spacing corresponds to the *a* dimension of orthoenstatite. It is probable that the blocks having spacings of 9 Å multiples are clinoenstatite irregularly interleaved between the regions of orthoenstatite. This, then, is presumably the origin of the stacking faults and the disorder that have been so widely discussed in the literature.

Some enstatite was synthetically heated and quenched. This experiment was performed in order to produce clinoenstatite. The resulting specimen indeed had many more regions of clinoenstatite, as well as a greatly increased density of stacking faults. An electron diffraction pattern (Fig. 13c) shows extensive streaking, reflecting the stacking faults. The indices on Figure 13c are for the orthoenstatite

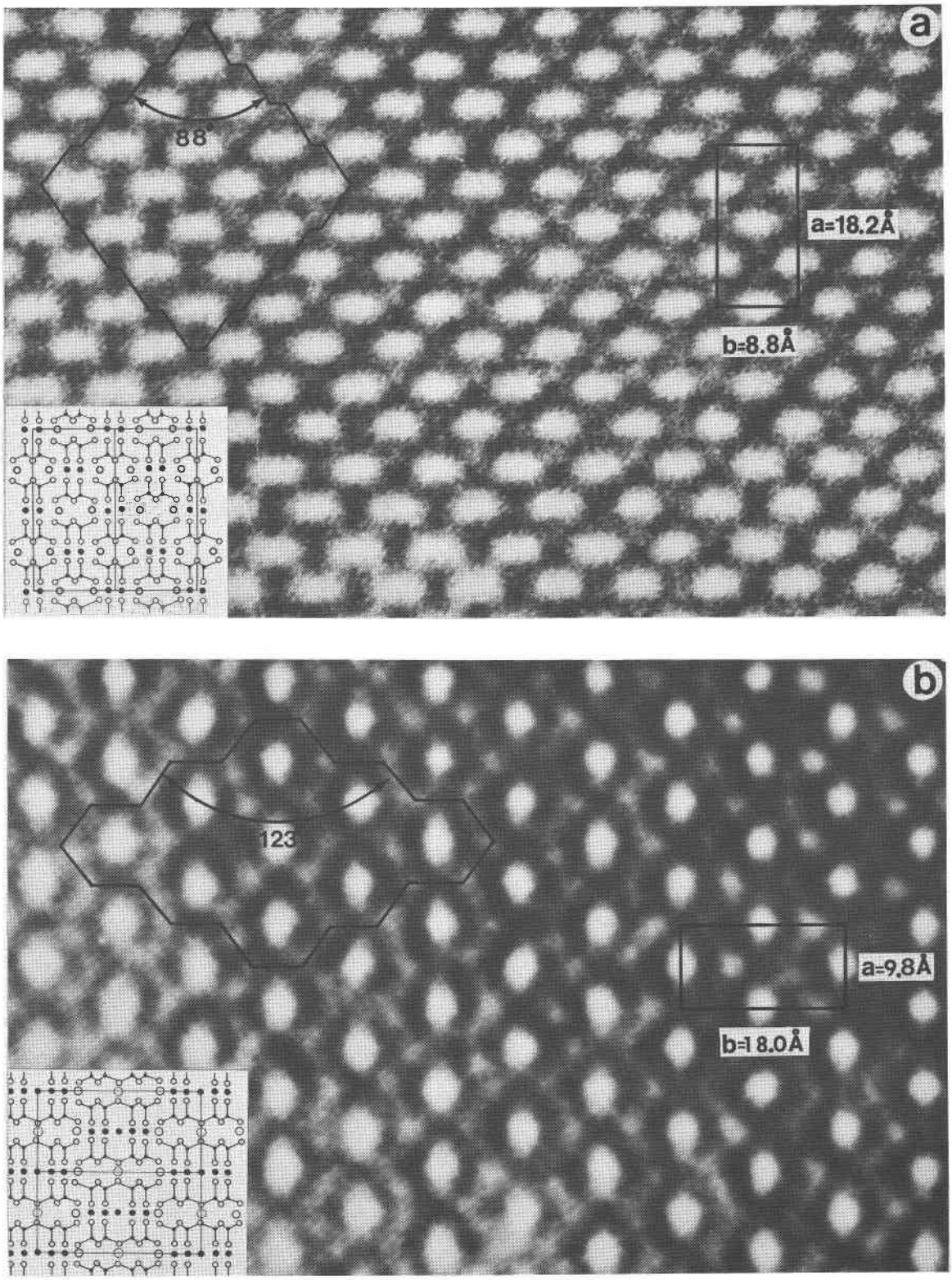

FIG. 11 a. High magnification structure image of an *a-b* section of orthoenstatite. The white regions correspond to the M_2 sites. A unit cell is outlined; the insert shows the orthoenstatite structure at the same scale as the electron image. Possible cleavage surfaces are sketched in the upper left. b. High magnification structure image of an *a-b* section of hornblende. The white regions correspond to the "*A*" sites. A unit cell is outlined; the insert shows the amphibole structure at the same scale as the structure image. Possible cleavage surfaces are sketched in the upper left.

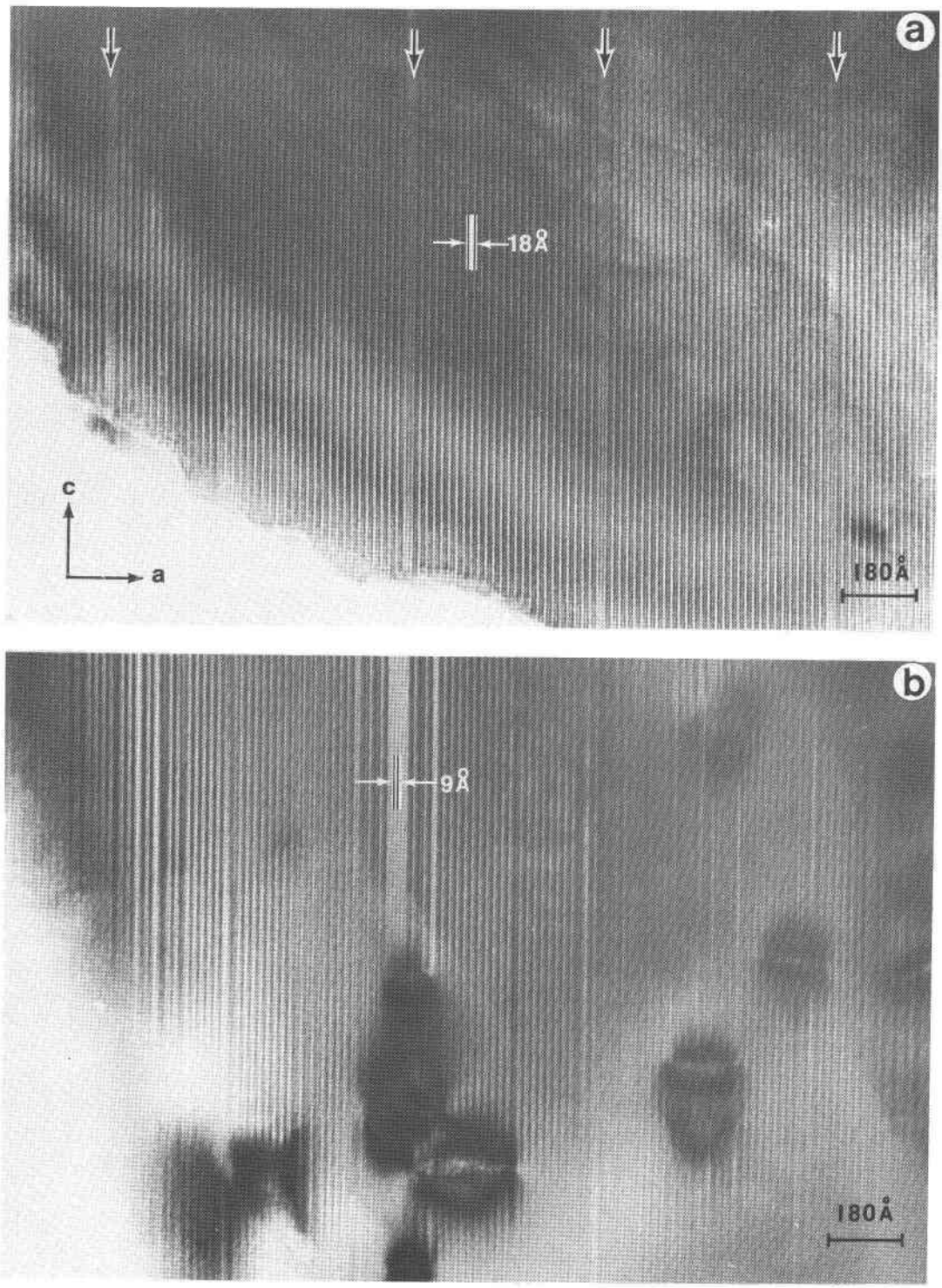

FIG. 12. a. Intermediate magnification structure image of an *a-c* section of enstatite showing parallel sets of fringes along *c*. Note the prominent irregularities produced by stacking faults between regions of ortho- and clino-enstatite.

b. Intermediate magnification structure image of an *a-c* section of artificially heated and quenched enstatite showing "discs" representing dislocation loops produced through radiation damage.

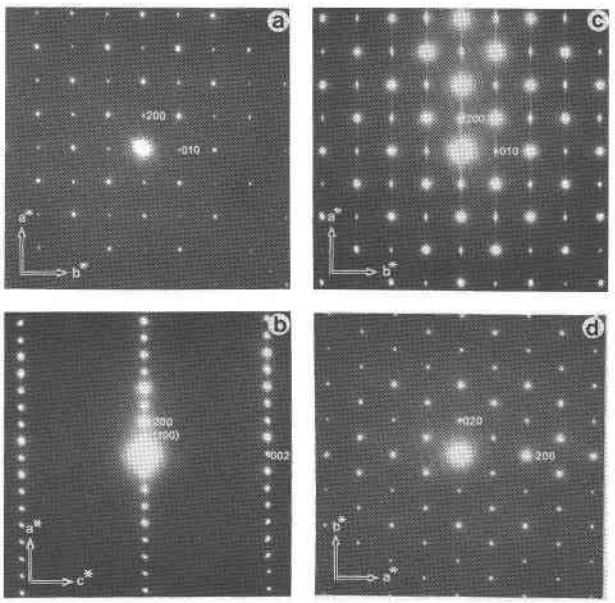

FIG. 13. Electron diffraction patterns showing:
a) *hk*0 reflections of orthoenstatite, corresponding to Figure 11a.
b) *h*0*l* reflections of orthoenstatite, corresponding to Figure 12a. Note the weak streaks parallel to a*; these are produced by the stacking faults seen in Figure 12a.
c) *hk*0 reflections of heated and quenched orthoenstatite containing appreciable regions of clinoenstatite; the 200 orthoenstatite reflection corresponds to the 100 clinoenstatite.
d) *hk*0 reflections of hornblende, corresponding to Figure 11b.

cell; 200 of orthoenstatite corresponds to 100 of clinoenstatite. When exposed to an intense electron beam this specimen developed dislocation loops (Fig. 12b). Such features were not observed in the unheated specimen. This, as well as the disorder and faults described above, will be described in more detail in a subsequent paper.

Hornblende

The essential features of the monoclinic amphiboles were first reported by Warren (1929). Amphiboles differ from pyroxenes in that their SiO_4 tetrahedra are linked into double rather than single infinite chains (Fig. 10b). The smaller cations such as Fe^{3+}, Fe^{2+}, Mg, and Mn fit into the M_1, M_2, and M_3 sites, whereas larger cations such as Ca and Na go into the M_4 sites. All of these sites are coplanar; M_1, M_2, and M_3 lie where the chains are "tip to tip" whereas M_4 lies closely adjacent. The largest cations such as K and Na fit into the "*A*" sites where the chains are "back to back". In some amphiboles some or all of the "*A*" sites are vacant.

The variety of hornblende that we studied is kaersutite, a Ca- and Ti-bearing amphibole derived from basaltic rocks. A detailed structural analysis of a kaersutite was recently reported by Kitamura and Tokonami (1971). They report $a = 9.81$, $b = 18.02$, and $c = 5.31$ Å, with space group $C2/m$. Our sample occurs as megacrysts in alkaline lavas apparently associated with the lherzolitic nodule locality at San Carlos, Arizona. Its composition, calculated on the the basis of an assumed weight ratio of $Fe^{2+}/\Sigma Fe = 0.75$, is shown in Table 1. Its formula is $(Na_{0.5}K_{0.2})\{Ca_{1.6}Na_{0.4}\}[Mg_{2.2}Fe^{2+}_{1.5}Fe^{3+}_{0.5}Ti_{0.5}Al_{0.3}](Al_{2.0}Si_{6.0})O_{22}(O, OH, F)_2$, for a ratio of $W:X:Y:Z = 0.7:2.0:5.0:8.0$.

Figure 11b shows the unit cell of hornblende in a structure image having *c* parallel to the electron beam. As in orthoenstatite, the white spots in hornblende occur where the chains are "back to back", *i.e.,* at the *"A"* sites, although in the case of the amphibole the spots are elongated in the orthogonal direction, pointing towards the hydroxyl and M_3 sites. The dark areas on either side of the white spots presumably correspond to M_4, the sites containing Ca. The zig-zag pattern of these shadows matches the positions of the M_4 sites parallel to *a*.

The long double chains characteristic of the amphiboles are shown in Figure 14a, where the crystal is oriented with a^* coincident with the electron beam. This photograph was taken through a relatively thick portion of the crystal and thus it is possible that the structure is not represented correctly. Nonetheless, the image corresponds closely to the theoretical structure. Note the hexagonal patterns, the long chains parallel to *c* and, in the *b* direction, the alternating light and dark areas corresponding to an intuitively reasonable structural representation. There is good correspondence with the appearance of an amphibole packing model. There is some ambiguity, however, as to whether the unit cell should be shifted by 4.5 Å parallel to [010]. This could be resolved by either doing a theoretical image contrast calculation or obtaining structure images of a crystal in which heavy atoms have been selectively substituted into particular sites.

As for enstatite, the cleavage of amphibole is well shown in the electron photomicrographs (Fig. 11b). Imperfections are also evident. Figure 14b shows what appear to be several antiphase domains. The inset details the discontinuity at the unit cell level.

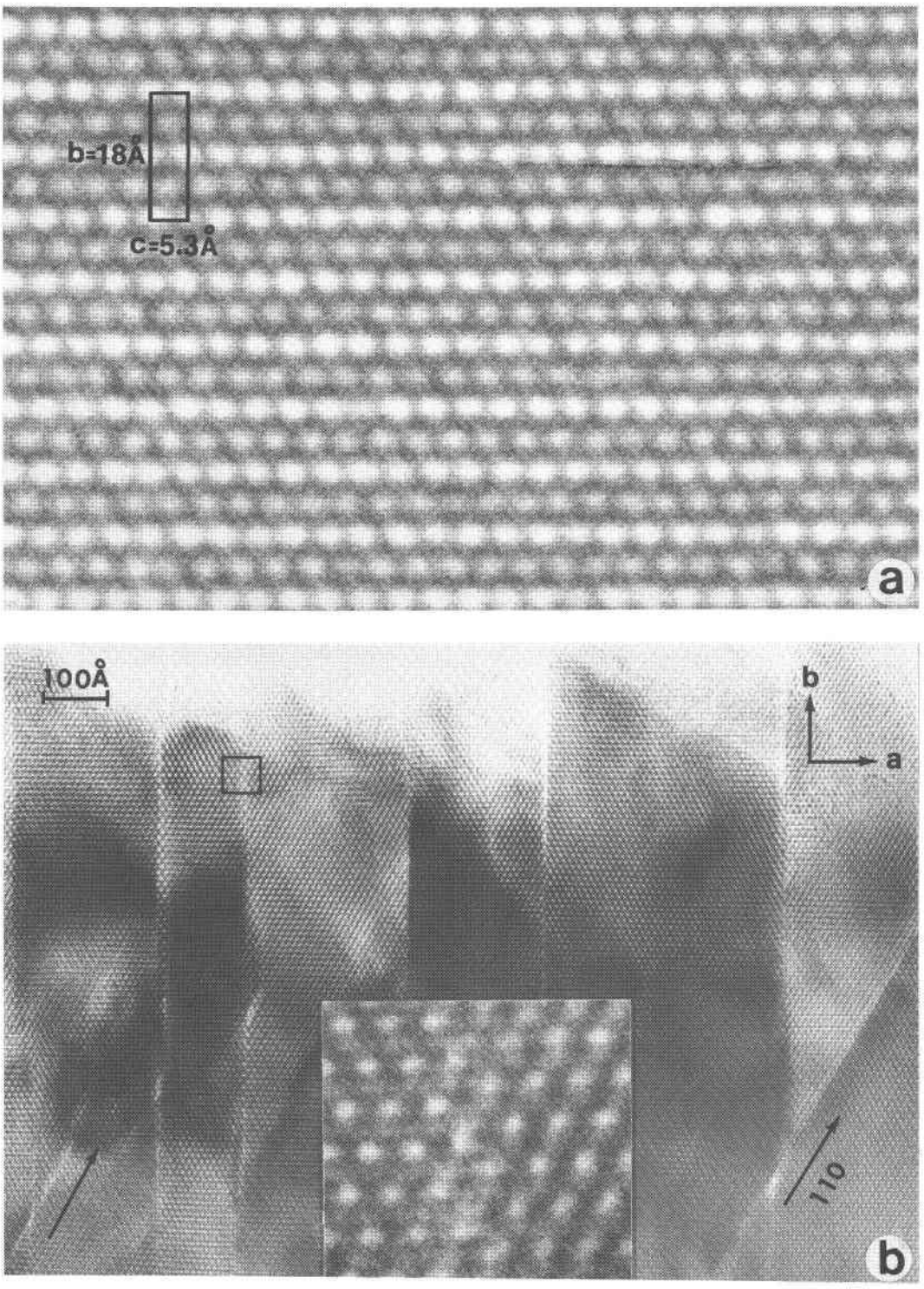

FIG. 14. a. Intermediate magnification structure image of a *b-c* section of hornblende showing the long double chains characteristic of the amphiboles. A unit cell is outlined.

b. Intermediate magnification structure image of an *a-b* section of hornblende showing several types of imperfections. The inset is an enlargement of the area outlined by the black square; it shows an antiphase boundary. Arrows indicate the traces of the cleavage planes.

A displacement vector having its trace along [120] appears to have been operative. It is not clear, however, that all of these (100) boundaries are antiphase. Note also that in the $a - b$ projection the white spots representing the "*A*" sites are not displaced across all of these boundaries.

The contrast differences on either side of some of the (100) boundaries are striking. They may well be the result of a slight structural mismatch producing a mosaic pattern. These boundaries are *not* parallel to the major amphibole cleavage planes. Their appearance may be compared to that of cleavage (Fig. 14b). Note that offset occurs wherever the cleavage planes cross the (100) boundaries, suggesting that the cleavage preceded or was displaced by some of the (100) boundaries. There is a possibility that the (100) boundaries were introduced during sample preparation, but this seems unlikely in view of their lack of coincidence with the prominent amphibole cleavage directions.

The orientation of the (100) boundaries of the hornblende is the same as the planar defects that are so pronounced in enstatite (Fig. 12a). In the latter case we believe these features result from the interleaving of plates having differing structures. It would indeed be interesting if related phenomena would occur in amphibole.

Scapolite

The structure of scapolite (Fig. 15a) consists of three-dimensionally linked SiO_4 tetrahedra, forming a framework structure having $a = 12.09$ and $c = 7.59$ Å. The larger cations, Ca and Na, fit into the elongate positions marked "S", and the large anions and radicals such as Cl, CO_3, SO_4 fit into the large cavities underlying the areas of four linked tetrahedra marked "R". Empty channels, "T", underlie groups of four linked tetrahedra that alternate with the "R" groups.

There is disagreement regarding its space group. Suggested groups include $I4/m$, $P4_2/n$, $P4_2/m$, $P4/m$, and $P4$ (Ulbrich, 1973). The last two groups are based on electron diffraction (Phakey and Ghose, 1972). Ulbrich suggests that the end members conform to $I4/m$ (see, for example, Papike and Zoltai, 1965; and Papike and Stephenson, 1966) while intermediate scapolites are $P4_2/n$.

We looked at a scapolite from Otter Lake, Quebec. Its composition (Table 1) conforms to the formula $(Ca_{1.9}Na_{1.8}K_{0.2})Al_{3.0}[Al_{1.3}Si_{7.7}O_{24}]Cl_{0.4}CO_{3_{0.4}}SO_{4_{0.1}}$. This lies almost in the center of the $Na_4Al_3(Si_9O_{24})Cl$–$Ca_4(Al_3Si_6O_{24})CO_3$ solid solution series, corresponding to Me_{49}, a dipyre bordering on mizzonite, according to the nomenclature of Shaw (1960).

A diffraction pattern taken with [010] as the zone axis shows the 100 and 001 reflections as weak spots. However, 001 is a forbidden reflection for space groups $P4_2/m$, $P4_2/n$, and $I4/m$ and so precludes these as the correct space groups. The presence of 100 also precludes $P4_2/n$ and $I4/m$. Supporting the above, it is of interest that 100 is systematically absent on certain other diffraction patterns, suggesting that there are structural variations within the crystal we studied. It would appear as if our data is consistent with and supportive of the data of Phakey and Ghose (1972) that suggests differing domains.

Figure 16 shows a structure image of scapolite oriented with *c* coincident with the electron beam. The large holes at the corners and center of the unit cell represent the "T" channels. The smaller white areas lying along the cell edge correspond to the "R" sites and the long, dark streaks oriented roughly in a cyclical fashion represent the elongate "S" positions.

The structure image of scapolite is less well defined than most of the other minerals shown in this paper. This "fuzziness" is a reflection of the fact that the scapolite is relatively unstable in the electron beam. It decomposes to form an amorphous region

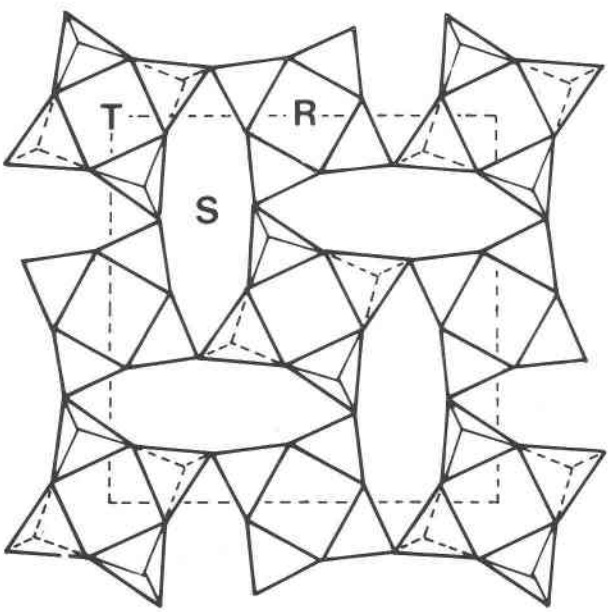

FIG. 15. The structure of a unit cell of scapolite, projected on (001) (after Schiebold and Seumel, 1932).

—clearly visible at the thin edges of the crystal but not shown in the figure. Such an edge and amorphous region is evident, however, in the lower right corner of Figure 9b. A similar amorphous layer presumably forms on the surface of the crystal and produces the slightly blurred image.

Muscovite

Figure 17a is an image of muscovite from Morristown, Arizona. The crystal is oriented with *a* and *b* perpendicular to the electron beam. Rather than necessarily indicating the true structure, this image simply reflects the hexagonal SiO_4 network characteristic of all of the sheet silicates. Presumably all would give similar patterns for this orientation. It should be pointed out that this image differs in some important respects from the other electron images shown in this paper. We have not confirmed that it was taken at the critical value of underfocussing, or that the image is of a sufficiently thin portion of the crystal. The resulting image is produced by sets of intersecting lattice fringes. These fringes correctly reflect crystal periodicities even though fine structural details do not appear. This detailing of periodicities is, in itself, an important advantage in those instances where there are variations in spacings. Care must be exercised, however, not to confuse fringes of this type with proper structural representations as shown in our other figures.

Figure 17b shows muscovite from the same locality "edge on", *i.e.*, with *c* lying in the plane of the photograph. The apparent major periodicity is approximately 10 Å, corresponding to the 1*M* polymorph (Smith and Yoder, 1956). They point out that, based on X-ray single crystal studies, this is a relatively unusual polymorph for muscovite. The crystal is very slightly tilted from the ideal orientation, making detailed interpretation of the fringes difficult. Nonetheless, there appears to be a reasonably good correspondence between the black fringes

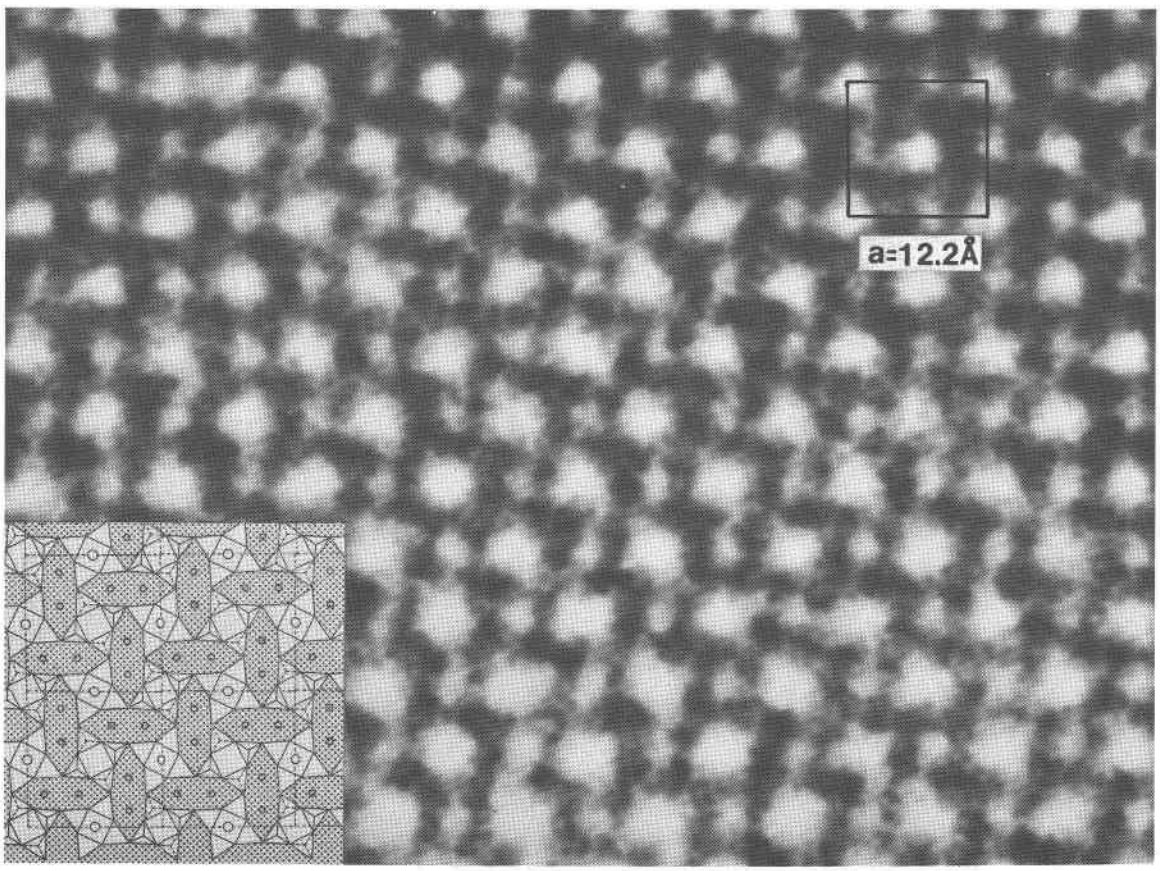

FIG. 16. High magnification structure image of scapolite. A unit cell is outlined; the insert shows the idealized structure from Figure 15a at the same scale as the electron image.

and the interlayer sites, and between the gray fringes and the intermediate tetrahedral and octahedral layers. If true, then this technique should permit relatively straightforward determination of mica polymorph type and stacking sequences, and provide material help in resolving some of the complexities of the sheet silicates.

Discussion and Conclusions

In the X-ray study of mineral structures we have been restricted to observing relatively large volumes (of the order of 10^{18} Å^3 or greater). High resolution electron microscopy radically changes this situation by permitting the imaging of portions of crystals having volumes up to 14 orders of magnitude smaller. This clearly provides much additional detail that was unavailable previously. The averaging of structure that is produced during X-ray diffraction obscures many features, some of which may have considerable geological significance. We expect the use of high resolution electron microscopy to obtain greatly increased structural detail that will provide much additional information regarding geochemical reactions and geological history.

The structure images shown on the preceding pages (1) confirm the considerable regularity of portions of many minerals, and (2) also show the variations on a unit cell level within certain minerals. High resolution electron microscopy is particularly well suited for the study of such defects. Details of the latter are not ascertainable with X-rays, but their significance may be considerable. Their implications are self-evident in terms of physical effects.

Minor structural variations have important chemical implications as well. For example, the intimate and coherent intergrowths of polymorphs such as ortho- and clinoenstatite in plates only one or a few unit cells wide raises interesting questions regarding the definition and, indeed, reality of single phases (or "monophasic assemblages"). Thermodynamic complications, perhaps only partly related to questions of equilibrium, are clearly raised if materials can only be considered monophasic on a unit cell by unit cell basis.

The ordering of defects, also best viewed by high resolution electron microscopy, similarly has chemical implications, in this instance by reflecting changes in the composition of crystals. It seems very likely that many regions of solid solution, so common in minerals of all sorts, may well be resolvable into discrete stoichiometric phases having only slightly differing compositions. To the extent that such small compositional changes reflect differences in the geological environment during the time of crystallization or later reequilibration, study of microscopic inhomogeneities in such phases has the potential of providing a whole new spectrum of geological information. For a review of defect ordering in synthetic phases see, for example, Eyring and Tai (1973).

Electron diffraction patterns and the corresponding image (not necessarily at high resolution) can be obtained in a matter of seconds from powder-sized crystals. This makes electron microscopy widely useful for mineralogical problems and permits relatively rapid space group assignments. "Forbidden"

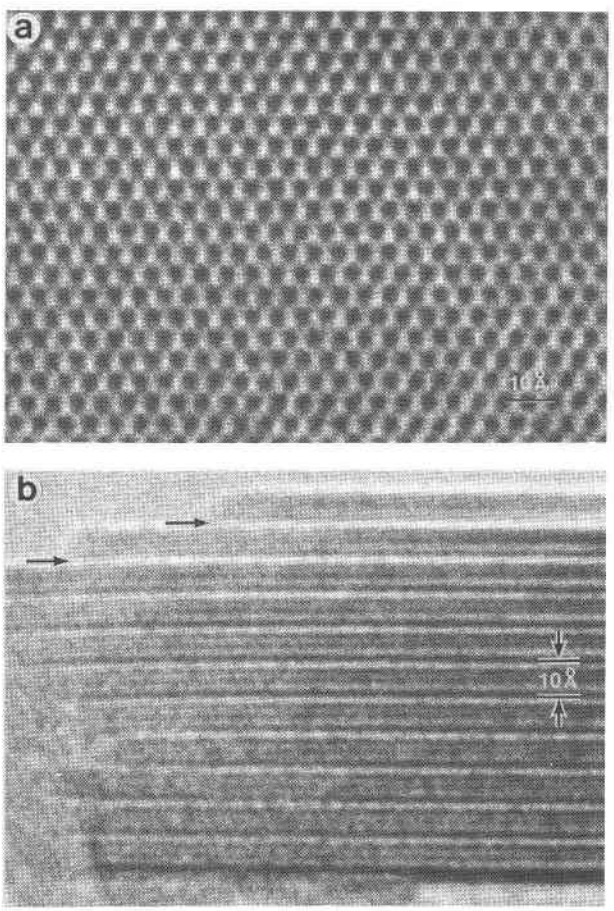

FIG. 17. a. Hexagonal array of muscovite having its *a* and *b* axes oriented perpendicular to the electron beam.

b. Muscovite orthogonally oriented to that in (a). Note the 10 Å stacking periodicity and the finer intermediate fringes, presumably corresponding to the layers of the tetrahedrally and octahedrally coordinated cations. The cleavage surfaces (indicated by arrows) are prominent.

spots in diffraction patterns of idocrase and scapolite result from antiphase domains and perhaps incorrect space group assignments. Those in enstatite are presumably produced by a combination of multiple diffraction and antiphase domains.

Aside from the above considerations, the main conclusions of this paper are:

1) Direct images of structural details can be obtained from silicates belonging to the main structural types. Corresponding diffraction patterns can be obtained rapidly and simply.
2) There are large areas of crystal that are free of major defects, *i.e.*, their projections show perfect periodicity on the scale of the resolution of the electron microscope.
3) Columns of tetrahedrally coordinated, cross linking Al and Si atoms (and their surrounding potential) can be imaged in cordierite. The ordering of cations should be resolvable in the near future.
4) Certain minerals are sensitive to radiation and thermal damage; idocrase and clinoenstatite show this to some degree. High voltage microscopy (~1MeV) may permit this problem to be diminished.
5) The resolution of defects such as stacking faults in enstatite may help explain structural problems of long standing. In this instance the supposed ambiguity between ortho- and clinoenstatite is explainable by the interlayering of plates several unit cells wide, *i.e.*, by having an intimate intergrowth even within "single" crystals.
6) The presence of "forbidden" spots in electron diffraction patterns is useful not only for space group determinations, but also for the detection of antiphase domains, presumably present in this case in idocrase, scapolite, and enstatite.
7) Physical properties, such as cleavage in the case of enstatite and hornblende, can be interpreted on the basis of electron images.
8) Stacking sequences and polymorphs in sheet silicates may be identified, and the study of these silicates advanced.
9) Single crystal data can be collected from the fine-grained powders which commonly result from experimental mineralogical and petrological studies.
10) Structural studies by X-rays can be greatly complemented by preliminary structure imaging and diffraction using electrons.

Acknowledgments

We thank Drs. J. Cowley, J. Holloway, G. S. Brown, and P. H. Ribbe for their helpful comments. Dr. Holloway and C. Lewis provided some samples; J. Armstrong, E. Holdsworth, J. Wheatley, and J. Steiner provided useful laboratory help. This study was supported in part by National Science Foundation grants GA25701 from the Earth Sciences Section, and GH3667 and GU3169. The latter two are a facility grant and an Area Development Grant in Solid State Science, respectively. Without these the facilities for this study would not have been available.

PRB also thanks the National Science Foundation for a Science Faculty Fellowship, and Professor J. S. Anderson for his hospitality and the opportunity to become familiar with electron microscopy during a year's stay at the Inorganic Chemistry Laboratory of Oxford University.

References Cited

ALLPRESS, J. G. (1970) Mixed oxides of titanium and niobium: Defects in quenched samples. *J. Solid State Chem.* **2,** 78–93.

———, AND J. V. SANDERS (1973) The direct observation of the structures of real crystals by lattice imaging. *J. Appl. Crystallogr.* **6,** 165–190.

———, ———, AND A. D. WADSLEY (1969) Multiple phase formation in the binary system Nb_2O_5–WO_3. VI. Electron microscopic observation and evaluation of non-periodic shear structures. *Acta Crystallogr.* **B25,** 1156–1164.

AREM, J. E., AND C. W. BURNHAM (1969) Structural variations in idocrase. *Am. Mineral.* **54,** 1546–1550.

BRAGG, W. L., AND J. WEST (1926) The structure of beryl $Be_3Al_2Si_6O_{18}$. *Proc. Roy. Soc. A,* **111,** 691–714.

BROWN, W. L., N. MORIMOTO, AND J. V. SMITH (1961) A structural explanation of the polymorphism and transitions of $MgSiO_3$. *J. Geol.* **69,** 609–616.

———, AND J. V. SMITH (1963) High temperature X-ray studies on the polymorphism of $MgSiO_3$. *Z. Kristallogr.* **118,** 186–212.

CODA, A., A. DELLA, G. ISETTI, AND F. MAZZI (1970) On the crystal structure of vesuvianite. *Atti Accad. Sci. Tor.* **105,** 1–24.

COWLEY, J. M., AND S. IIJIMA (1972) Electron microscope image contrast for thin crystals. *Z. Naturforsch.* **27,** 445–451.

———, AND A. F. MOODIE (1957) The scattering of electrons by atoms and crystals. I. A new theoretical approach. *Acta Crystallogr.* **10,** 609–619.

EYRING, L., AND L. TAI (1973) The structural chemistry of some complex oxides. Ordered and disordered extended defects, in *Treatise on Solid State Chemistry,* Vol. III. Plenum Press, New York.

FONTAINE, F. (1969) Transformations ordre-désordre de la cordiérite. *Z. Kistallogr.* **129,** 271–279.

GIBBS, G. V. (1966) The polymorphism of cordierite. I: The crystal structure of low cordierite. *Am. Mineral.* **51,** 1068–1087.

———, D. W. BRECK, AND E. P. MEAGHER (1968) Structural refinement of hydrous and anhydrous synthetic beryl, $Al_2(Be_3Si_6)O_{18}$ and emerald, $Al_{1.9}Cr_{0.1}(Be_3Si_6)O_{18}$. *Lithos,* **1,** 275–285.

GOSSNER, B., AND F. MUSSGNUG (1928) Vergleichende röntgenographische Untersuchung von Magnesiumsilikaten. *Neus Jahrb. Mineral. (A),* **58,** 213–227.

IIJIMA, S. (1971) High resolution electron microscopy of crystal lattice of titanium-niobium oxide. *J. Appl. Phys.* **42,** 5891–5893.

———, AND J. G. ALLPRESS (1973) Structural studies by high resolution electron microscopy: Tetragonal tungsten bronze-type structures in the system Nb_2O_5–WO_3. *Acta Crystallogr.* (in press).

———, S. KIMURA, AND M. GOTO (1973) Direct observation of point defects in $Nb_{12}O_{29}$ by high resolution electron microscopy. *Acta Crystallogr.* (in press).

———, J. M. COWLEY, AND G. DONNAY (1973) High resolution microscopy of tourmaline. *Tscher. Mineral. Petrol. M.H.* (in press).

ITO, J., AND J. E. AREM (1970) Idocrase: synthesis, phase relations, and crystal chemistry. *Am. Mineral.* **55,** 880–912.

KITAMURA, M. AND M. TOKONAMI (1971) The crystal structure of kaersutite. *Sci. Rep. Tohoku Univ. Ser. 3,* **11,** 125–141.

LANGER, K., AND W. SCHREYER (1969) Infrared and powder X-ray diffraction studies on the polymorphism of cordierite, $Mg_2(Al_4Si_5O_{18})$. *Am. Mineral.* **54,** 1442–1459.

MEAGHER, E. P., AND G. V. GIBBS (1965) Crystal structure and polymorphism of cordierite (abstr.) *Geol. Soc. Ann. Meetings,* Kansas City, Missouri.

MIYASHIRO, A. (1957) Cordierite-indialite relations. *Am. J. Sci.* **255,** 43–62.

PAPIKE, J. J., AND T. ZOLTAI (1965) The crystal structure of a marialite scapolite. *Am. Mineral.* **50,** 641–655.

———, AND N .C. STEPHENSON (1966) The crystal structure of mizzonite, a calcium- and carbonate-rich scapolite. *Am. Mineral.* **51,** 1014–1027.

PHAKEY, P. P., AND S. GHOSE (1972) Scapolite: observation of antiphase domain structure. *Nature Phys. Sci.* **238,** 78–80.

POLLACK, S. S. (1966) Disordered orthopyroxene in meteorites. *Am. Mineral.* **51,** 1722–1726.

———, AND W. D. RUBLE (1964) X-ray identification of ordered and disordered ortho-enstatite. *Am. Mineral.* **49,** 983–992.

REID, A. M., AND A. J. COHEN (1967) Some characteristics of enstatite from enstatite achondrites. *Geochim. Cosmochim. Acta,* **31,** 661–672.

SCHIEBOLD, E., AND G. SEUMEL (1932) Über die Kristallostruktur von Skapolith. *Z. Kristallogr.* **81,** 110–134.

SHAW, D. M. (1960) The geochemistry of scapolite. I. Previous work and general mineralogy. *J. Petrology,* **1,** 218–260.

SMITH, J. V. (1969) Crystal structure and stability of the $MgSiO_3$ polymorphs; Physical properties and phase relations of Mg, Fe pyroxenes. *Mineral. Soc. Am. Spec. Pap.* **2,** 3–29.

———, AND H. S. YODER, JR. (1956) Experimental and theoretical studies of the mica polymorphs. *Mineral. Mag.* **31,** 209–235.

TURNER, F. J., H. HEARD, AND D. T. GRIGGS (1960) Experimental deformation of enstatite and accompanying inversion to clinoenstatite. *XXI Int. Geol. Cong. Copenhagen,* **18,** 399–408.

ULBRICH, H. H. (1973) Crystallographic data and refractive indices of scapolites. *Am. Mineral.* **58,** 81–92.

WARREN, B. E. (1929) The structure of tremolite $H_2Ca_2Mg_5(SiO_3)_8$. *Z. Kristallogr.* **72,** 42–57.

———, AND D. I. MODELL (1931) The structure of vesuvianite $Ca_{10}Al_4(Fe,Mg)_2Si_9O_{34}(OH)_4$. *Z. Kristallogr.* **78,** 422–432.

YADA, K. (1971) Study of the microstructure of chrysotile asbestos by high resolution microscopy. *Acta Crystallogr.* **A27,** 659–664.

YOSHIDA, T., AND E. SUITO (1972) Interstratified layer structure of organo-montmorillonites as revealed by electron microscopy. *J. Appl. Crystallogr.* **5,** 119–124.

ZOLTAI, T. (1960) Classification of silicates and other minerals with tetrahedral structures. *Am. Mineral.* **45,** 960–973.

Manuscript received, August 2, 1973; accepted for publication, October 2, 1973.